

# Measurement of Non-Monotonic Runaway Electron Distributions in Tokamaks and their Dependence on Plasma Parameters

C. Paz-Soldan,<sup>1,\*</sup> C. M. Cooper,<sup>2</sup> P. Aleynikov,<sup>3</sup> D. C. Pace,<sup>1</sup> N. W. Eidietis,<sup>1</sup> D. P. Brennan,<sup>4</sup>  
R. S. Granetz,<sup>5</sup> E. M. Hollmann,<sup>6</sup> C. Liu,<sup>4</sup> A. Lvovskiy,<sup>2</sup> R. A. Moyer,<sup>6</sup> and D. Shiraki<sup>7</sup>

<sup>1</sup>*General Atomics, San Diego, CA, USA*

<sup>2</sup>*Oak Ridge Associated Universities, Oak Ridge, TN, USA*

<sup>3</sup>*Max-Planck Institute for Plasma Physics, Greifswald, Germany*

<sup>4</sup>*Princeton University, Princeton, NJ, USA*

<sup>5</sup>*Massachusetts Institute of Technology, Cambridge MA, USA*

<sup>6</sup>*University of California-San Diego, La Jolla, CA, USA*

<sup>7</sup>*Oak Ridge National Laboratory, Oak Ridge, TN, USA*

(Dated: December 25, 2016)

Novel spatial, temporal, and energetically resolved measurements of bremsstrahlung hard X-ray (HXR) emission from runaway electron (RE) populations in tokamaks reveal non-monotonic RE distribution functions whose properties depend on the interplay of electric field acceleration with collisional and synchrotron damping. Measurements are consistent with theoretical predictions of momentum-space attractors that accumulate runaway electrons. RE distribution functions are measured to shift to higher energy when the synchrotron force is reduced by decreasing toroidal magnetic field strength. Increasing collisional damping by increasing electron density (at fixed magnetic and electric field) reduces the energy of the non-monotonic feature and reduces the HXR growth rate at all energies. Higher energy HXR growth rates extrapolate to zero at the expected threshold electric field for RE sustainment while low energy REs are anomalously lost. Compilation of HXR emission from different sight-lines into the plasma yields energy and pitch-angle resolved RE distributions and demonstrates increasing pitch-angle and radial gradients with energy.

*Introduction* Reaching mega-ampere currents and mega-electron volt (MeV) energies during fast shutdown events, runaway electrons (REs) pose perhaps the greatest operational risk to tokamak fusion reactors such as ITER [1–4]. Due to the severe potential for damage to the reactor walls, opportunities for empirical tuning of RE control actuators will be limited. Instead, a first-principles predictive understanding is needed, and present-day experiments fill a crucial need in validating theoretical predictions of RE dissipation.

Classical theories for relativistic RE generation in tokamaks based on the effects of Coulomb collisions (small angle [5] and secondary avalanche [6]) determine the critical electric field ( $E_C$ ) for the growth of RE populations. Further work highlighted the important role of synchrotron damping in elevating the threshold electric field above  $E_C$  [7, 8], and several experiments have since yielded evidence of the elevated threshold [9–12]. These observations motivated the development of a rigorous analytical theory [13] and computational tools [14–19] that clarified the importance of the effects of pitch-angle scattering and synchrotron damping. Alongside quantifying the enhancement of the threshold field, these works predict phase-space circulation patterns resulting in a pile-up of REs at specific energies potentially resulting in non-monotonic features in the RE distribution function ( $f_e$ ). While important to the RE dissipation rate and thus the prospects for control, neither have these features of  $f_e$  been directly observed nor has a detailed model validation of experimental  $f_e$  together with dissipation rates been made until now.

In this Letter we report the first spatially, energetically, and temporally resolved reconstructions of  $f_e$  in tokamaks and their dependence on plasma parameters. The effect of varying synchrotron and collisional damping on  $f_e$  is directly shown and direct comparisons to time-dependent modeling are made. This significantly expands on previous measurements [20–22] by spatially localizing the RE emission, isolating the synchrotron effect, and comparing directly to modeling. Experiments are conducted using trace RE populations in low-density Ohmic plasmas [11] in the DIII-D tokamak with parameters targeted to non-dimensionally match the expected conditions in post-disruption RE beams in ITER, with both predicted to develop non-monotonic  $f_e$ . Non-monotonic features at the predicted energies are observed and their dependence on synchrotron and collisional damping rates will be described.

*Measurement Technique* Emission from RE populations are measured using a novel toroidally-viewing (tangential) pinhole camera made entirely of lead, pictured in Fig. 1(a) and described in detail in Refs. [23, 24]. Bremsstrahlung radiation emitted when a RE scatters off a plasma ion or neutral is collimated into the discrete sight-lines of the camera. Due to the tangential view only emission from low pitch-angle REs is measured. The sight-lines view different parts of the plasma cross-section, shown in Fig. 1(b). Along each sight-line, different angles are made between the equilibrium magnetic field direction ( $\hat{b}$ , obtained from equilibrium reconstructions) and the sight-line orientation ( $\hat{k}$ ). The minimum

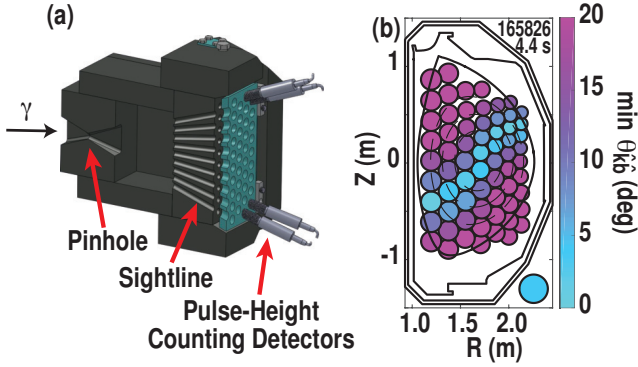


FIG. 1. (a) Lead pinhole camera geometry and (b) sight-lines into the plasma at the tangency plane. Colors indicate the minimum angle ( $\theta_{\hat{k}\hat{b}}$ ) between the magnetic field orientation ( $\hat{b}$ ) and the sight-line orientation ( $\hat{k}$ ). The lower-right circle in (b) denotes a full-view sightline.

$\theta_{\hat{k}\hat{b}}$  along the sight-line is used to color code the view. Emission along each active sight-line is measured by a Bismuth-Germanate (BGO) scintillating crystal together with a photodiode. The scintillation pulses from individual photons are digitized at 10 MHz sample rate, with the pulse height determining the photon energy ( $E_\gamma$ ). Binning the pulse heights in time allows an energy spectrum of HXR photons ( $f_\gamma$ ) to be assembled.  $f_\gamma$  is a convolution of  $f_e$ , the bremsstrahlung emission coefficients [25], and Compton scattering in the scintillator [26]. Assuming spatial homogeneity of  $f_e$ , knowledge of the bremsstrahlung emission and Compton scattering allows inversion of  $f_\gamma$  to  $f_e$  by computing the expected  $f_\gamma$  from a set of mono-energetic  $f_e$ . In the inversions finite pitch-angle effects are ignored thus only 1-D experimental  $f_e$  are shown.

**Background Plasma and Modeling Framework** The quiescent flat-top scenario is employed [11]. Initial low density operation builds a robust (and monotonic) RE population due to primary (Dreicer) production that also undergoes secondary avalanche. When the REs reach a critical intensity, an asynchronous trigger at  $t_{\text{puff}}$  begins the RE dissipation phase. Here, background plasma properties such as the toroidal magnetic field ( $B_T$ ) and the electron density ( $n_e$ ) are actuated independently [shown in Fig. 2(a)] to vary the RE damping terms and study their effect on  $f_e$ . Primary production ceases in the dissipation phase as thermal transport changes reduce the electron temperature. Note the dimensional  $B_T$  and  $n_e$  map to changes in the synchrotron and collisional damping terms, and are non-dimensionalized by the parameters  $\hat{\tau}_r \equiv \frac{3}{2} \left( \frac{m_e \ln \Lambda}{\epsilon_0} \right) \frac{n_e}{B_T^2} \approx 28 \frac{n_e [10^{19} \text{m}^{-3}]}{(B_T [\text{T}])^2}$ , the ratio of the collision to the synchrotron damping time), and  $E/E_C \equiv \frac{4\pi\epsilon_0^2 m_e V_C^2}{n_e e^3 \ln \Lambda} \approx 10 \frac{V_{\text{loop}} [\text{V}]}{n_e [10^{19} \text{m}^{-3}]}$ , the ratio of the toroidal electric field to the critical field).  $E$  is measured at the plasma surface but any radial gradients relax quickly ( $< 1$  s) compared to discharge time scales. The ion charge  $Z$  is also measured with charge exchange

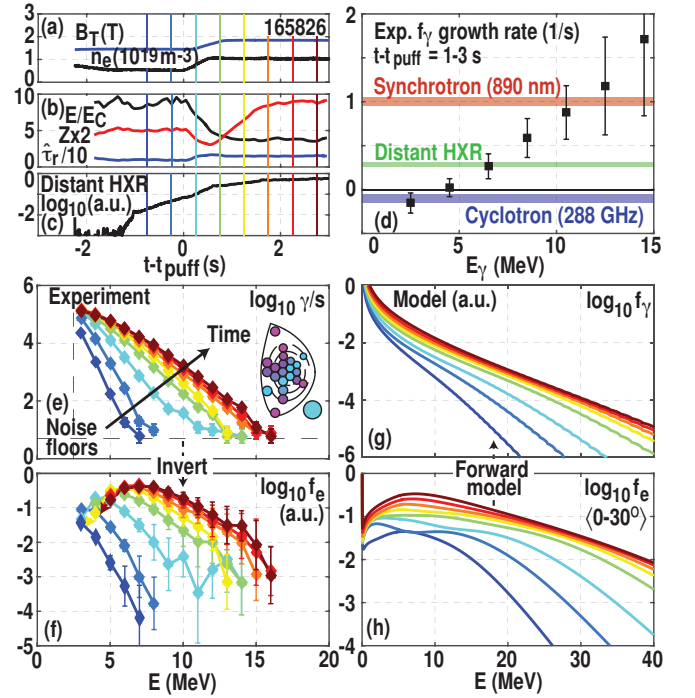


FIG. 2. (a) Experimental actuators, (b) non-dimensional parameters, and (c) distant HXR signal for a typical discharge. (d-e) measured  $f_\gamma$  shows increasing growth rate as energy increases, and flattening at mid-energy consistent with (f) non-monotonic  $f_e$  feature formation. (g-h) Model predictions of  $f_\gamma$  and  $f_e$  are broadly consistent with the data.

spectroscopy and actuated by replacing deuterium ions ( $Z=1$ ) with nitrogen ions ( $Z=7$ ) holding  $n_e$  constant. The plasma retains keV thermal temperatures and is thus fully ionized, so no corrections due to bound electrons are needed. The non-dimensional  $E/E_C$ ,  $Z$ , and  $\hat{\tau}_r$  accessed are similar to expected values in ITER thus giving access to ITER-relevant RE dissipation regimes.

To model the evolution of  $f_e$  the time-dependent relativistic 2D Fokker-Planck equation (ex. Ref. [27]) is solved numerically inputting measured on-axis (spatially 0-D) plasma parameters [Fig. 2(b)]. The equation as in Ref. [13] is solved with two amendments: 1) the collision operator is extended to be valid for lower energies (similar to Refs. [28, 29]) and 2) an approximate secondary source is included which captures the effect of a finite energy incident electron population. This treatment accurately captures the analytical results of RE generation models [5, 6, 30] as well as the near-threshold regime [13]. The computed  $f_e$  evolution is then placed through a forward model taking into account bremsstrahlung emission coefficients and sight-line geometry to obtain the predicted  $f_\gamma$  [24]. Unlike inversion from  $f_\gamma$  to  $f_e$ , forward modeling from  $f_e$  to  $f_\gamma$  requires no assumptions, though in accordance with the tangential view only the low pitch-angle part of the distribution  $\langle 0-30^\circ \rangle$  is used in the  $f_\gamma$  calculation (though taken to have zero pitch-angle).

*Global Distribution Measurement* The discharge in Fig. 2 accesses strong synchrotron damping ( $\hat{\tau}_r \approx 15$ ), high  $Z$  ( $\approx 4$ ), and modest collisional damping ( $E/E_C \approx 4$ ) [Fig. 2(a,b)]. For these parameters, the total HXR energy flux measured on a distant plastic scintillator [Bicron BC-400, Fig. 2(c)] grows. Measurements (here aggregating all spatial channels) find very different  $f_\gamma$  growth rates with HXR energy ( $E_\gamma$ ) [Fig. 2(d)]. Comparison of growth rates across emission bands are consistent. At low  $E_\gamma$  ( $\leq 2$  MeV),  $f_\gamma$  decays together with 288 GHz electron cyclotron emission (ECE), as expected since ECE is dominated by low energy REs. Similarly, high  $E_\gamma$  growth rates match that of visible synchrotron emission (SE) at 890 nm, as expected since SE is dominated by high-energy ( $>10$  MeV) REs [31]. The growth rate of the distant HXR detector is skewed to low  $E_\gamma$ , indicating that this type of diagnostic (often used to infer RE population) does not clearly discriminate between RE energy and population.

Measurements of  $f_\gamma$  and inversion to  $f_e$  [Fig. 2(e,f)] reveal  $f_\gamma$  changes at mid-energy which upon inversion map to the development of a non-monotonic  $f_e$  from an originally peaked  $f_e$ . Modeling of this same discharge to predict  $f_e$  and forward model  $f_\gamma$  [Fig. 2(g,h)] indicates a similar evolution is predicted. As with experiment,  $f_\gamma$  increases more rapidly at high energy, and a non-monotonic feature in  $f_e$  is computed for these experimental conditions at a similar energy ( $\approx 7$  MeV). The final  $f_e$  shape is near-stationary, indicating the phase-space circulation effect gives rise to the non-monotonic feature. Note the absence of  $f_e$  points late in time below 5 MeV is due to the prediction of slightly negative  $f_e$  (with large uncertainty) due to the subtractions involved in the inversion process, indicating that while the degree of hollowness is difficult to quantify, peaked  $f_e$  are excluded. Additionally, two experimental noise floors are present: at low flux due to limited counting statistics ( $\leq 5\gamma/s$ ), and at low energy due to pulse heights approaching electronic noise levels ( $\leq 1$  MeV). Modeled  $f_e$  are momentum-space distributions plotted against energy, are normalized such that  $n_{RE} = \int f_e dp$ , and are directly comparable to experiment. Modeled  $f_\gamma$  take units  $[\gamma/\text{MeV s}]$ , while experimental  $f_\gamma$  are direct  $\gamma/s$  count rate histograms with uniform 1 MeV binning. Note a non-monotonic  $f_e$  using this normalization does not necessarily imply kinetic instability drive, though the  $f_e$  in Fig 2(h) also meets this criteria. **DOES IT?**

*Angular and Spatial Dependencies* Comparison of  $f_\gamma$  from individual sight-lines allows extraction of radial and pitch-angle profiles of RE distributions. This is due to the emission angular localization provided by the relativistic forward-beaming effect. For a sight-line with a low minimum  $\theta_{\hat{k}\hat{b}}$ , emission will be dominated by near-zero pitch-angle REs. However, sight-lines with non-zero minimum  $\theta_{\hat{k}\hat{b}}$  will predominantly see REs whose pitch angle roughly matches  $\theta_{\hat{k}\hat{b}}$  for sharp emission cones.

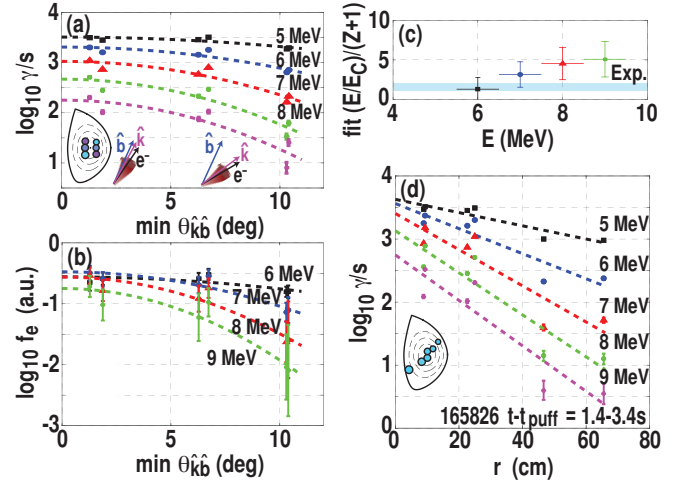


FIG. 3. Angular and spatial RE distribution dependency for the same discharge of Fig. 2. Experimental (a-b)  $f_\gamma$  and  $f_e$  show reductions at high  $\theta_{\hat{k}\hat{b}}$ , allowing (c) inference of  $E/E_C$  to  $(Z+1)$  according to Ref. [13]. (d) Energy-dependent  $f_\gamma$  radial falloff is also observed.

Thus, comparing  $f_\gamma$  from sight-lines viewing the same flux surface at different minimum  $\theta_{\hat{k}\hat{b}}$  is roughly equivalent to resolving the  $f_\gamma$  pitch-angle distribution. An example pitch-angle resolved  $f_\gamma$  measurement is shown in Fig. 3(a), plotting against the minimum  $\theta_{\hat{k}\hat{b}}$  and illustrating energy-dependent fall-off. Note 10 MeV emission cones are narrower than minimum  $\theta_{\hat{k}\hat{b}}$  separation (see cartoon), though blurring does occur below 5 MeV, setting a low  $E_\gamma$  angular resolution limit.  $f_\gamma$  from each sight-line can be inverted [Fig. 3(b)], confirming expectations of a more forward beamed  $f_e$  at higher energy. The inferred  $f_e$  pitch-angle dependence can be compared to theoretical predictions [13] of exponential angle fall-off with a decay coefficient proportional to the ratio of  $E/E_C$  to  $Z+1$ . As shown in Fig. 3(c), the prediction is within experimental uncertainty though a discrepancy is found at high energy. Note the error bars are larger for this measurement due to lower counting statistics for single sight-lines. With improved statistics, the high- $E_\gamma$  formulation of Ref. [8] may also be validated. Future work will also pursue 2-D (angle-resolved)  $f_e$  inversions.

Individual sight-lines with the same low minimum  $\theta_{\hat{k}\hat{b}}$  but viewing different flux surfaces can also be used to measure radial profiles of  $f_\gamma$ , as shown in Fig. 3(d). As with the pitch-angle distribution, radial fall-off is more pronounced at high energy, indicating energy-dependent spatial transport is present.

*Global Parametric Dependencies* Modifying the synchrotron and collisional damping rate is found to have a strong effect on the measured  $f_\gamma$  and  $f_e$  in both theory and experiment (aggregating now over all active sight-lines). The effect of synchrotron radiation is isolated by using three matched discharges with similar pre-histories and post-puff parameters ( $E/E_C = 3.1 \pm 0.3$  and  $Z = 1.4 \pm 0.1$ ) but varying  $B_T$ , thus accessing a wide

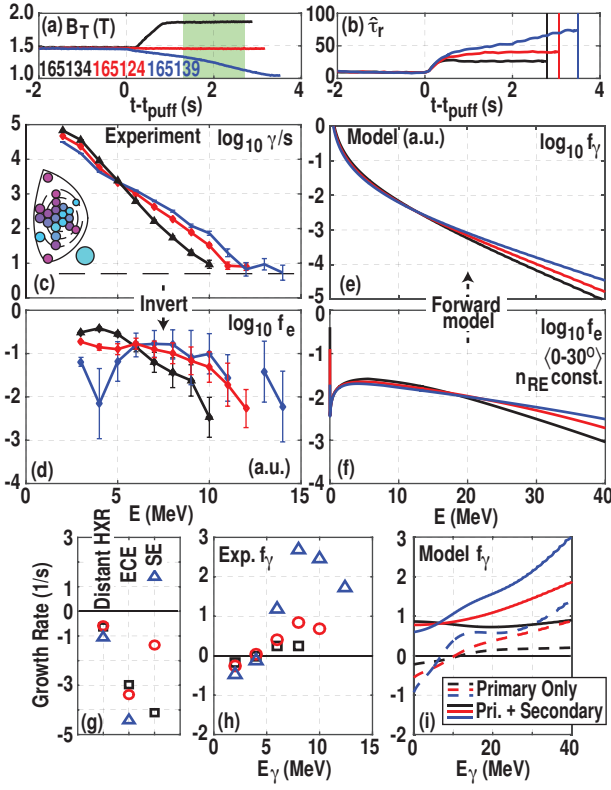


FIG. 4. Effect of modifying synchrotron force on RE distributions actuated through (a) varying the toroidal field ( $B_T$ ) resulting in a wide change in  $\hat{\tau}_r$  (b). Measured (c)  $f_\gamma$  and (d)  $f_e$  from the green interval in (a) show an expansion to high energy and contraction at low energy. Model (e)  $f_\gamma$  and (f)  $f_e$  show qualitative similarity, normalizing to constant  $n_{RE}$ . Growth rate analysis for (g) other diagnostics, (h) experimental  $f_\gamma$ , and (i) model  $f_\gamma$  are also shown.

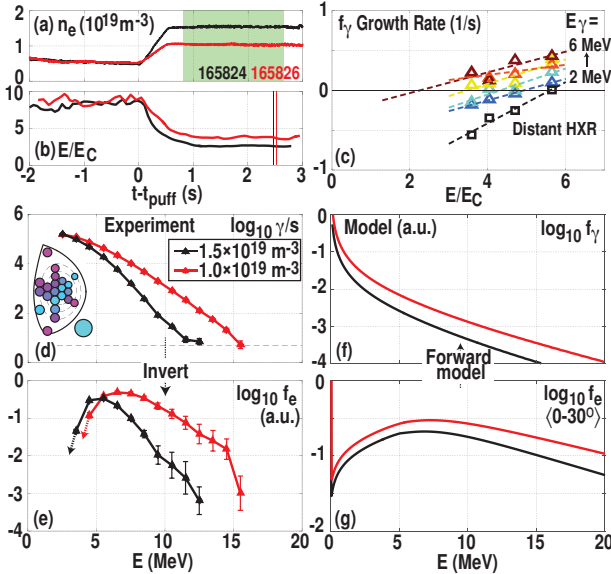


FIG. 5. Effect of modifying collisional damping by increasing (a)  $n_e$  resulting in (b) a decrease in  $E/E_C$ . Measured (c)  $f_\gamma$  and (d)  $f_e$  from the green interval in (a) indicate that RE energization is inhibited, consistent with model predicted (e)  $f_\gamma$  and (f)  $f_e$ . (g)  $f_\gamma$  growth rates indicate high-energy REs decay at a lower  $E/E_C$  than low energy REs.

range of  $\hat{\tau}_r$  [Fig. 4(a-b)]. Experimental  $f_\gamma$  [Fig. 4(c)] demonstrate a reduction in high  $E_\gamma$  counts and an increased spectral index as  $B_T$  is raised, opposite to the expectation from single-particle confinement arguments, yet consistent with synchrotron effects limiting the high-energy  $f_e$ . Interestingly, at low  $E_\gamma$  a decrease in  $f_\gamma$  is found with decreasing  $B_T$ . Experimental  $f_e$  [Fig. 4(d)] indicates the RE distribution is getting progressively flatter as  $B_T$  is decreased, with the lowest  $B_T$  displaying a non-monotonic feature in  $f_e$  outside of experimental uncertainty. Modeling of these cases [Fig. 4(e-f)] qualitatively predicts the observed shape variations with  $\hat{\tau}_r$ . However, variations between  $f_e$  and  $f_\gamma$  at different  $\hat{\tau}_r$  are observed at lower energy than in modeling, indicating a stronger  $B_T$  effect in experiment potentially due to the neglect of spatial effects. Indeed, the input on-axis  $B_T$  value is lower than the inboard value, which is also where visible synchrotron emission is known to be localized [11, 31].

Considering emission growth rates [Fig. 4(g,h)] the distant HXR, ECE, and low  $E_\gamma$   $f_\gamma$  growth rates all decrease with increasing  $B_T$ . In contrast, SE and high  $E_\gamma$   $f_\gamma$  rates display the opposite  $B_T$  trend. All emissions are thus broadly consistent a shift to high energy as  $B_T$  is lowered. Note however quantitative ECE and SE growth rates differ from the  $f_\gamma$  rates, due to the direct  $B_T$  dependencies of these emissions. The corresponding model-predicted  $f_\gamma$  growth rates are shown in Fig. 4(i). Agreement is good at high  $E_\gamma$ , though at low  $E_\gamma$  the observed decay is not reproduced unless the secondary source term is artificially removed as might be expected if  $E/E_C$  were somewhat lower.

Increasing collisional damping by raising  $n_e$  thus decreasing  $E/E_C$  [Fig. 5(a-b)] is found to decrease the growth rate of HXR emission [Fig. 5(c)] across all  $E_\gamma$ . Growth rates of all other measured emissions (ECE, SE, distant HXR) also decrease as  $E/E_C$  is reduced (not shown). A transition from HXR signal growth to decay at  $E/E_C$  far above  $E/E_C=1$  is measured on the distant plastic scintillator (as reported in Refs. [11, 12]) but the  $E_\gamma$  dependence of this diagnostic is unclear.  $E_\gamma$  resolved measurements reveal increasing HXR growth rate with  $E_\gamma$  at fixed  $E/E_C$  [also seen in Fig. 4(h)]. Thus, the  $E/E_C$  value where HXR growth transitions to decay decreases with increasing  $E_\gamma$ . While extrapolation is necessary to find this value at high energy, it is roughly at  $E/E_C \approx 2$ . This compares more favorably to the threshold field for RE generation which is predicted to be at  $E/E_C=1.6$  for these conditions [13], indicating a more consistent behavior at high energy. Comparison of experimental and model  $f_\gamma$  and  $f_e$  [Fig. 5(d-g)] show good agreement, with the high  $E/E_C$  case extending to higher energy and with a harder spectral index than at low  $E/E_C$ . The experimental non-monotonic feature increases in energy from 5 to 7 MeV as  $E/E_C$  is raised, also in good agreement with model predictions (from 6

to 7 MeV).

*Summary and Conclusion* Comparing experimental and modeled  $f_e$ , nearly all qualitative trends are captured: 1) both develop non-monotonic features at consistent energy, 2)  $f_e$  are more parallel-directed at high energy, 3) increasing synchrotron damping (lowering  $\hat{\tau}_r$ ) shifts  $f_e$  towards lower energy, 4) increasing collisional damping (lowering  $E/E_C$ ) decreases  $f_e$  at all energies. The  $f_e$  shape and location of non-monotonic features are generally in agreement as  $E/E_C$  and  $\hat{\tau}_r$  are varied. A notable exception to the wide qualitative agreement between experiment and theory is the behavior at low energy, where systematically lower  $f_\gamma$  growth rates are observed. The cause remains unknown, but may be due to spatial transport effects not included in the 0-D model [32]. Spatial effects may also cause the quantitatively stronger effect of  $B_T$  seen in experiment.

To conclude, novel measurements provide first confirmation of non-monotonic features in RE distribution functions and their dependence on collisional and synchrotron damping terms. The broad agreement found validates the importance of these effects and improves confidence that these models can be used to design optimized RE mitigation strategies. Looking forward, the identified discrepancies will guide improvements to RE dissipation models and enable improved validation against the spatial, temporal, pitch-angle, and energetic effects described herein.

The authors thank M. Austin, S. Haskey, B. Grierson, and Y. Zhu for diagnostic support, as well as N. Commaux, and A. Wingen for their assistance, and T. Fülöp, O. Embréus, A. Stahl, and G. Wilkie for useful discussions.

---

\* paz-soldan@fusion.gat.com

- [1] T. C. Hender et. al, Nucl. Fusion **47**, S128 (2007).
- [2] M. Lehnén et. al, J. of Nucl. Mat. (2014), 10.1016/j.jnucmat.2014.10.075.
- [3] E. M. Hollmann et. al, Phys. Plasmas **22**, 021802 (2015).
- [4] A. H. Boozer, Phys. of Plasmas **22** (2015), 10.1063/1.4913582.
- [5] J. W. Connor and R. J. Hastie, Nucl. Fusion **15**, 415 (1975).
- [6] M. N. Rosenbluth and S. V. Putvinski, Nucl. Fusion **37**, 1355 (1997).
- [7] J. R. Martin-Solis, J. D. Alvarez, R. Sanchez, and B. Esposito, Phys. of Plasmas **5**, 2370 (1998).
- [8] F. Andersson, P. Helander, and L. G. Eriksson, Phys. of Plasmas **8**, 5221 (2001).
- [9] J. R. Martin-Solis, R. Sánchez, and B. Esposito, Physical Review Letters **185002**, 9 (2010).
- [10] E. M. Hollmann et. al, Nucl. Fusion **51**, 103026 (2011).
- [11] C. Paz-Soldan, N. W. Eidietis, R. S. Granetz, E. M. Hollmann, R. A. Moyer, N. A. Crocker, A. Wingen, and Y. Zhu, Phys. Plasmas **21**, 022514 (2014).
- [12] R. S. Granetz, B. Esposito, J. H. Kim, R. Koslowski, M. Lehnén, J. R. Martin-Solis, C. Paz-Soldan, T. Rhee, J. C. Wesley, L. Zeng, and I. M. Group, Phys. Plasmas **21**, 072506 (2014).
- [13] P. B. Aleynikov and B. N. Breizman, Physical Review Letters **114**, 155001 (2015).
- [14] P. B. Aleynikov, K. Aleynikova, B. N. Breizman, G. T. A. Huijsmans, S. V. Konovalov, S. V. Putvinski, and V. Zhogolev, in *Proc. of 25th IAEA Fusion Energy Conf. (St. Petersburg, Russia)* (2014) pp. TH/P3–38.
- [15] E. Hirvijoki, I. Pusztai, J. Decker, O. Embréus, A. Stahl, and T. Fülöp, J. Plasma Phys. **81**, 475810502 (2015).
- [16] A. Stahl, E. Hirvijoki, J. Decker, O. Embréus, and T. Fülöp, Phys. Rev. Lett. **114**, 115002 (2015).
- [17] C. Liu, D. P. Brennan, A. H. Boozer, and A. Bhattacharjee, Phys. Plasmas **2**, 1 (2015).
- [18] J. Decker, E. Hirvijoki, O. Embréus, Y. Peysson, A. Stahl, I. Pusztai, and T. Fülöp, Plasma Phys. Contr. Fusion **58**, 025016 (2016).
- [19] C. Liu, D. P. Brennan, A. H. Boozer, A. Bhattacharjee, Plasma Physics and Controlled Fusion **59**, 024003 (2017).
- [20] A. E. Shevelev, E. M. Khilkevitch, V. G. Kiptily, I. N. Chugunov, D. B. Gin, D. N. Doinikov, V. O. Naidenov, A. E. Litvinov, and I. A. Polunovskii, Nucl. Fusion **53**, 123004 (2013).
- [21] A. E. Shevelev, E. M. Khilkevitch, S. I. Lashkul, V. V. Rozhdestvensky, and A. B. Altukhov, Nucl. Instruments and Methods in Physics Research A **830**, 102 (2016).
- [22] E. M. Hollmann, P. B. Parks, N. Commaux, N. W. Eidietis, R. A. Moyer, D. Shiraki, M. E. Austin, C. J. Lasnier, C. Paz-Soldan, and D. L. Rudakov, Phys. Plasmas **22**, 056108 (2015).
- [23] D. C. Pace, C. M. Cooper, D. Taussig, N. W. Eidietis, E. M. Hollmann, V. Riso, and M. A. V. Zeeland, Rev. Sci. Instrum. **87**, 043507 (2016).
- [24] C. M. Cooper, D. C. Pace, N. Commaux, N. W. Eidietis, E. M. Hollmann, and D. Shiraki, Rev. Sci. Instrum. **87**, 11E602 (2016).
- [25] H. W. Koch and J. W. Motz, Rev. Mod. Phys. **31**, 920 (1959).
- [26] Y. Peysson and F. Imbeaux, Rev. Sci. Instrum. **70**, 3987 (1999).
- [27] L.-G. Eriksson and P. Helander, Computer Physics Communications **154**, 175 (2003).
- [28] P. Helander, *Collisional Transport in Magnetized Plasmas* (Cambridge University Press, 2002).
- [29] G. Papp, M. Drevlak, T. Fülöp, and P. Helander, Nucl. Fusion **51**, 43004 (2011).
- [30] P. B. Parks, M. Rosenbluth, and S. Putvinski, Phys. Plasmas **6** (1999), 10.1063/1.873524.
- [31] J. H. Yu, E. M. Hollmann, N. Commaux, N. W. Eidietis, D. A. Humphreys, A. N. James, T. C. Jernigan, and R. A. Moyer, Phys. Plasmas **20**, 042113 (2013).
- [32] P. Helander, L.-G. Eriksson, and F. Andersson, Physics of Plasmas **7**, 4106 (2000).